Journal of Power Sources 269 (2014) 651–660

Contents lists available at ScienceDirect

Journal of Power Sources

journal homepage: www.elsevier.com/locate/jpowsour

Organic–inorganic hybrid polymer electrolytes based on polyether diamine, alkoxysilane, and trichlorotriazine: Synthesis, characterization, and electrochemical applications

Diganta Saikia [a], Cheng-Gang Wu [a], Jason Fang [b], Li-Duan Tsai [b], Hsien-Ming Kao [a, *]

[a] Department of Chemistry, National Central University, Chung-Li 32054, Taiwan, ROC
[b] Department of Fuel Cell Materials and Advanced Capacitors, Division of Energy Storage Materials and Technology, Material and Chemical Laboratories, Industrial Technology Research Institute, Hsin-Chu 300, Taiwan, ROC

HIGHLIGHTS

- A hybrid electrolyte was developed based on ED2003, alkoxysilane, and trichlorotriazine.
- Solid hybrid electrolyte exhibits ionic conductivity up to 1.6×10^{-4} S cm^{-1} at 30 °C.
- Electrochromic device exhibits coloration efficiency of 183 cm^2 C^{-1} and over 200 cycles.
- Initial discharge capacity value of 100 mAh g^{-1} is obtained from battery testing.

GRAPHICAL ABSTRACT

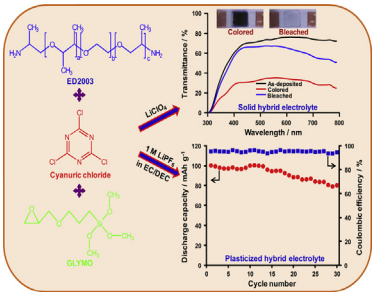

ARTICLE INFO

Article history:
Received 24 March 2014
Accepted 30 June 2014
Available online 7 July 2014

Keywords:
Organic–inorganic hybrid polymer electrolyte
Ionic conductivity
Solid-state nuclear magnetic resonance
Electrochromic device
Lithium-ion battery

ABSTRACT

A new type of highly conductive organic–inorganic hybrid polymer electrolytes has been synthesized by the reaction of poly(propylene glycol)-*block*-poly(ethylene glycol)-*block*-poly(propylene glycol) bis(2-aminopropyl ether), 2,4,6-trichloro-1,3,5-triazine and alkoxysilane precursor 3-(glycidyloxypropyl)trimethoxysilane, followed by doping of $LiClO_4$. The ^{13}C and ^{29}Si solid-sate NMR results confirm the successful synthesis of the organic–inorganic hybrid structure. The solid hybrid electrolyte thus obtained exhibits a maximum ionic conductivity of 1.6×10^{-4} S cm^{-1} at 30 °C, which is the highest among the organic–inorganic hybrid electrolytes. The hybrid electrolytes are electrochemically stable up to 4.2 V. The prototype electrochromic device with such a solid hybrid electrolyte demonstrates a good coloration efficiency value of 183 cm^2 C^{-1} with a cycle life over 200 cycles. For the lithium-ion battery test, the salt free solid hybrid membrane is swelled with a $LiPF_6$-containing electrolyte solution to reach an acceptable ionic conductivity value of 6.5×10^{-3} S cm^{-1} at 30 °C. The battery cell carries an initial discharge capacity of 100 mAh g^{-1} at 0.2C-rate and a coulombic efficiency of about 95% up to 30 cycles without the sign of cell failure. The present organic–inorganic hybrid electrolytes hold promise for applications in electrochromic devices and lithium ion batteries.

1. Introduction

The ever-increasing global energy demand and depletion of fossil fuels have increased the awareness towards sustainable energy sources. However, uncontrollable and intermittent natures of

* Corresponding author. Tel.: +886 3 4275054; fax: +886 3 4227664.
E-mail address: hmkao@cc.ncu.edu.tw (H.-M. Kao).

http://dx.doi.org/10.1016/j.jpowsour.2014.06.159
0378-7753/

these sources augmented the need for an efficient energy storage system. Electrochemical devices which can store energy and/or convert energy are mainly composed of electrolyte and electrodes, and the performance of these devices depends on the exploitation of each components. In electrolytes category, polymer electrolyte is one of the promising research areas that attracted ever-increasing interests due to its potential applications in electrochemical devices, such as, solid state rechargeable lithium or lithium-ion batteries, dye-sensitized solar cells, supercapacitors, electrochromic devices, sensors, etc. [1–4]. Depending on their physical properties, polymer electrolytes can be categorized as solid, gel, plasticized, rubbery and composite polymer electrolytes. Solid polymer electrolytes (SPEs) are the materials of interests for several decades due to the advantages they possess in comparison to other types of electrolytes. The study of solid polymer electrolytes was first reported by Wright's group in 1973 with lithium salt complexes with poly(ethylene oxide) [5]. Later, Armand et al. highlighted the possible application of these polymer-salt complexes as battery electrolytes [6]. Although the ionic conductivity of SPEs is not up to the mark compared to gel or plasticized polymer electrolytes, the mechanical stability and structural integrity make SPEs more suitable for applications in electrochemical devices. On the other hand, liquid electrolytes are always a source of cell leakage and can cause safety problems [7]. Significant efforts have been devoted by research groups worldwide to enhance the room temperature ionic conductivity of SPEs by a variety of approaches, such as blending of polymers, co-polymerization, cross-linking, and addition of nano/micron sized filler particles [8–12]. Apart from these strategies, another convenient approach to improve the electrochemical properties is the development of the organic–inorganic hybrid electrolytes or so-called organically modified electrolytes (i.e., Ormolytes) [13–17]. These organic–inorganic hybrid materials are advantageous due to the easy control of the properties of the final material by controlling the chemical nature of the organic and inorganic phases, the size and morphology of these domains, and the nature of the interphase interactions. The sol–gel process employed for their syntheses allows a wide variation in compositions and inorganic/organic ratios, together with an excellent control of porosity and functional groups. Moreover, the versatile nature of the organic–inorganic matrix allows it to be prepared for both solid and plasticized hybrid electrolytes, which has tremendously increased its usage in electrochemical devices.

With the primary goal of developing a highly conductive hybrid electrolyte, herein a new type of organic–inorganic electrolyte was synthesized by the reaction of 2,4,6-trichloro-1,3,5-triazine (cyanuric chloride, CC) with poly(propylene glycol)-*block*-poly(-ethylene glycol)-*block*-poly(propylene glycol) bis(2-aminopropyl ether) (ED2003), followed by the reaction with 3-(glycidyloxypropyl)trimethoxysilane (GLYMO). Cyanuric chloride was used as the core because of its ability to form a star-branched structure. The CC core units provide cross-linking centers by reacting and replacing the chloride atoms with amine ended ED2003 polymer chain to make a branched cross-linked structure. The PEG and PPG parts of ED2003 polymer help to enhance the ionic conductivity and mechanical strength of the hybrid electrolyte, respectively. GLYMO provides a cross-linking unit through a sol–gel process to increase the mechanical strength of the hybrid by forming a silicate network structure. The CC/ED2003 ratio was adjusted in the hybrid structure in order to achieve the best ion conducting product. The silicate network makes the membrane mechanically stable and gives the composite nature to the membrane by forming *in-situ* sub-micron sized particles. Besides, the salt-free hybrid membrane can be further swelled in electrolyte solvents to enhance the ionic conductivity. The thermal behavior and electrochemical properties of the hybrid electrolytes are characterized by various experimental techniques. To the end, the prototype electrochromic devices and Li-ion batteries are fabricated by using these hybrid electrolytes to demonstrate their potential applications.

2. Experimental section

2.1. Materials

Lithium perchlorate ($LiClO_4$), lithium trifluoromethanesulfonate (LiOTf), lithium bis(trifluoromethylsulfonyl) imide (LiTFSI) and triblock copolymer H_2N-$(PPG)_a(PEG)_b(PPG)_cNH_2$ (commercially designated by Jeffamine ED2003 with M_w = 2000 g mol^{-1} containing $a+c = 6$; $b = 39$) were purchased from Aldrich and dried at 70 °C for 24 h under vacuum prior to their use. Cyanuric chloride (CC, Aldrich) and GLYMO (Aldrich) were used as received. Ethylene carbonate (EC) and propylene carbonate (PC) were obtained from Alfa Aesar. The electrolyte of 1 M $LiPF_6$ in EC/diethyl carbonate (DEC) was acquired from Tomiyama Chemicals, Japan. Lithium foil from Alfa Aesar was used as anode. The cathode material $Li(Ni_{0.4}Mn_{0.4}Co_{0.2})O_2$ (NMC-442) was provided by the Industrial Technology Research Institute (ITRI) in Taiwan. Tungstic acid powder (Riedel-de Haën) and hydrogen peroxide (H_2O_2, Aldrich) were used as received. A nontoxic and biodegradable surfactant Brij 56 [$C_{16}H_{33}(OCH_2CH_2)_{10}OH$] was purchased from Aldrich and used as received. Indium tin oxide (ITO) glass sheet with 7 Ω resistances was acquired from AimCore Technology Co., Ltd., Taiwan. Tetrahydrofuran (THF) was distilled from sodium/benzophenone prior to use.

2.2. Preparation of the star-branched organic–inorganic hybrid electrolytes

To prepare the solid hybrid electrolytes, $LiClO_4$ and ED2003 were dried under vacuum for 2 days prior to use. Scheme 1 illustrates the synthesis procedures of the star-branched organic–inorganic hybrids. The synthesis of the hybrid electrolyte was carried out by selecting different molar ratios of CC and ED2003 following the procedures as described by Jan et al. [18] to control the total units of CC and ED2003 in the hybrid structure. In a typical synthesis, appropriate amounts of CC and ED2003 were dissolved separately in THF, and then mixed together under stirring for 24 h at 25 °C. The mixture was made considering the CC/ED2003 ratios of 1/2, 3/4, 5/6, 7/8, 9/10 (i.e., N/N + 1) in the first step. In the second step, the temperature of the mixture was raised to 130 °C and another 1 equivalent (N) of ED2003 monomer was added for the 1/2 mixture and stirred continuously for 24 h. Similarly, for the 3/4, 5/6, 7/8, and 9/10 mixtures, further we added 3, 5, 7, and 9 equivalents of the ED2003 monomer, respectively, to complete the coupling reaction that substitutes the chloride from the CC ring. In the third step, the temperature of the solution was brought down to 25 °C, and then added 3 equivalents of GLYMO (for other ratios, it was N + 2), and continuously stirred for 24 h further to react with the remaining amine end of ED2003 of the 1/2 mixture to form the organic–inorganic hybrid structure. Finally, the reaction temperature was maintained at 25 °C and appropriate amounts of $LiClO_4$ were added into the solution to achieve the desired [O]/[Li] ratios and stirred for another 24 h. The resulting viscous solution was cast onto Teflon dishes and dried under a reduced pressure at 70 °C for 2 days to get a transparent and crack-free film with good mechanical strength and a good degree of elasticity. All the procedures and material handlings were carried out in a glove box filled with an argon atmosphere. The solid hybrid electrolytes were designated as CEG(N)–*X*, where C represents the cyanuric chloride, E corresponds to the parent polymer ED2003, G denotes the GLYMO, and *X*

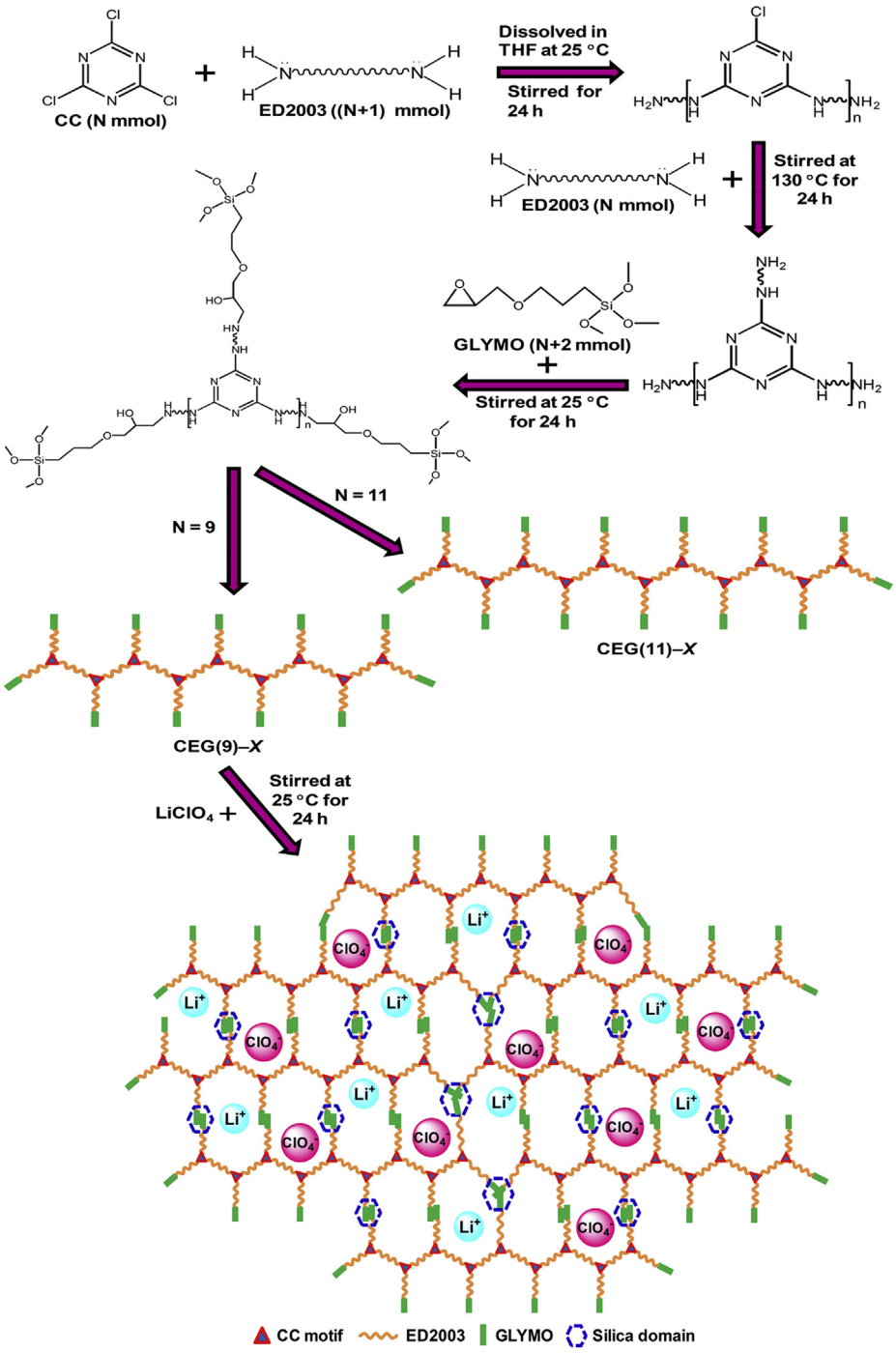

Scheme 1. Schematic representation for the synthesis of organic–inorganic hybrid electrolyte.

indicates the number of ether oxygen atoms (only for polymer) per Li^+ cation, that is, [O]/[Li]. N can be considered as the number of the CC unit. The thickness of the films was controlled to be in the range of 70–90 μm.

In order to reach the ionic conductivity for the Li-ion battery test, the salt free membrane CEG(9)–∞ was swelled in different electrolyte solvents, such as 1 M $LiClO_4$ in EC/PC (1:1 v/v), 1 M LiOTf in EC/PC (1:1 v/v), 1 M $LiPF_6$ in EC/DEC (1:1 v/v) and 1 M LiTFSI in EC/PC (1:1 v/v) and formed the "plasticized" hybrid electrolytes. The thickness of plasticized hybrid electrolyte membranes was in the range of 50–60 μm.

2.3. Preparation of electrochromic film

The WO_3 film was prepared by the procedures described in our previous paper [19]. Briefly, 1 g of Peroxotungstic acid (PTA) flakes was dissolved in a mixture of deionized H_2O and ethanol. The ratio of deionized H_2O and ethanol in the mixture was chosen to be 2:1. Then, 0.2 g of H_2O_2 was added with the PTA solution to enhance the stability of the solution. The surfactant solution was prepared by adding 0.2 g of Brij 56 in 2.5 g deionized H_2O and 1.25 g of ethanol. Final coating sol was prepared by slowly adding the surfactant solution to the PTA solution under stirring. The sol was drop-casted

on cleaned ITO glass substrates and dried at room temperature for 6 h. The coated glasses were annealed at 190 °C for 1 h and subsequently treated at 350 °C for 2 h to remove the template and very fine WO_3 coated films were obtained. The WO_3 coated ITO glasses were stored in the glove box to fabricate electrochromic devices.

2.4. Fabrication of electrochromic devices

Electrochromic devices were assembled in a sandwich like structure by applying a small amount of the CEG(9)–*X* hybrid electrolyte solution onto the surface of WO_3 deposited ITO glass. Then, the hybrid electrolyte layer deposited electrochromic glass slide was dried under vacuum at 70 °C for 2 days. A second ITO-coated glass slide was placed on top of the dried electrolyte layer and the two slides were pressed together and kept for 1 h to spread the electrolyte film in between them and for good contacts. Afterwards, the device was sealed with adhesive in the sides and wrapped up the un-deposited part of the ITO glass with copper tape for good electrical contacts.

2.5. Assembling of lithium ion batteries

A standard 2032 coin-cell hardware was used for the assembling of the lithium ion battery. Lithium metal was used as the anode. The cathode was prepared by blade-coating a slurry of 88 wt.% $Li(Ni_{0.4}Mn_{0.4}Co_{0.2})O_2$ (NMC-442), 3 wt.% super P carbon, 3 wt.% carbon black and 6 wt.% poly(vinylidene fluoride) (PVdF) binder in *N*-methyl-2-pyrrolidone (NMP) on aluminum foil, drying overnight at 120 °C in an oven, roller-pressing the dried coated foil, and punching out circular discs. The highest ion conducting CEG(9)–∞ hybrid membrane with 1 M $LiPF_6$ in EC/DEC was used as the electrolyte. The lithium ion battery was assembled by sandwiching the plasticized hybrid electrolyte between the lithium anode and NMC-442 cathode.

2.6. Characterization methods

The thermal property of the CEG(9)–*X* electrolytes was measured by differential scanning calorimetry (DSC) in the temperature range from −60 to 120 °C using Perkin–Elmer Pyris 6 DSC at a heating rate of 10 °C min^{-1}. The sample weights were maintained in the range of 7–8 mg and were hermetically sealed in aluminum pans. The reported DSC curves were the second heating scans taken after an initial heating scan to erase the thermal history, followed by quenching to −60 °C. The glass transition (T_g) and melting temperatures (T_m) were measured, and the associated enthalpy changes (ΔH) were calculated.

Fourier transform infrared (FTIR) spectra were obtained from a Bio-Rad FTS155 spectrometer over the range of 4000–500 cm^{-1} at a resolution of 4 cm^{-1} using the KBr wafer technique. Band deconvolution of the resulting spectra in the range of 600–650 cm^{-1} was conducted with Gaussian–Lorentzian functions to obtain the best fit for the band envelope.

Solid-state NMR experiments were performed on a Varian Infinityplus-500 NMR spectrometer, equipped with a Chemagnetics 7.5 or 5 mm magic angle spinning (MAS) T3 probe. The Larmor frequencies for ^7Li, ^{13}C, and ^{29}Si nuclei are 194.3, 125.7 and 99.3 MHz, respectively. The Hartmann–Hahn matching condition for $^1H \rightarrow {}^{13}C$ cross-polarization (CP) MAS experiments was determined using admantane. ^{13}C and ^{29}Si chemical shifts were externally referenced to tetramethylsilane (TMS) at 0 ppm.

AC impedance measurements of the CEG(N)–*X* electrolytes were performed using Autolab/PGSTAT302 (Metrohm Autolab B.V., Netherlands) frequency response analyzer over a frequency range of 1 Hz–100 kHz with an amplitude of 10 mV. All the specimens were sandwiched by two polished stainless steel (SS) blocking electrodes in argon atmosphere inside a glove box (Innovative technology, PL-HE-2GB with PL-HE-GP1 inert gas purifier) for conductivity tests. The measurements were performed in the temperature range of 15–80 °C, and the system was thermally equilibrated at each selected temperature for at least one hour. Complex impedance plots were computed from the experimental data. The intercept at the real impedance axis in the Nyquist plots corresponds to the bulk electrolyte resistance (R_b) and hence the ionic conductivity values (σ) are obtained from equation $\sigma = (1/R_b)(t/A)$, where t is the thickness of the electrolyte film and A is the area of the electrode.

Linear sweep voltammetry (LSV) measurement was carried out in CEG(9)–*X* solid hybrid electrolyte systems with various [O]/[Li] ratios and CEG(9)–∞ plasticized hybrid electrolyte systems with different electrolyte solvents. A standard 2032 coin-cell hardware was used for cell fabrication. The CEG(9)–*X* electrolytes were dried overnight at 70 °C in an oven and placed into an argon-filled glove box that contained <1 ppm oxygen and moisture. In the case of plasticized hybrid electrolytes, the dried CEG(9)–∞ (salt free) membranes were dipped in different electrolyte solvents for 60 min before assembling the cell. The electrochemical stability of the hybrid polymer electrolytes was determined by LSV using stainless steel (SS) as a working electrode and lithium as counter and reference electrodes for a Li/hybrid polymer electrolyte/SS cell at a scan rate of 1 mV s^{-1} from an open circuit potential to 6 V vs. Li/Li^+.

The optical transmittance was measured using a UV–Vis double beam spectrophotometer (T90+, PG Instruments) over the wavelength range from 300 to 800 nm. Cyclic voltammetry measurements were carried out in Autolab/PGSTAT302 electrochemical analyzer with a scan rate of 30 mV s^{-1}.

Chronoamperometric (CA) measurements of the electrochromic device with the solid hybrid electrolyte were performed using Autolab/PGSTAT 302 by monitoring the device current response as a function of time while the applied voltage was stepped between −3.0 V and +3.0 V with a delay time at each voltage of 50 s. The WO_3 coated ITO glass substrate was used as a working electrode and another ITO glass acted as the counter and reference electrodes. The cathodic and anodic charge densities were determined through the integration of the CA curves during the coloring and bleaching processes.

Charge–discharge studies were carried out with WonATech WBCS3000 automatic battery cycler. Lithium metal and NMC-442 were used as the anode and cathode, respectively. The cycle tests of normal charge were carried out at a 0.2 C-rate between 2.8 and 4.0 V.

3. Results and discussion

To achieve the highest ionic conductivity by optimizing the CC/ED2003 ratios, the hybrid systems of CEG(5) to CEG(11) were doped with $LiClO_4$ with a [O]/[Li] ratio of 32. It was found that initially the ionic conductivity increased with the increase in the CC/ED2003 ratios (Fig. S1, Supplementary Information, SI) and reached the maximum value for CEG(9). When the CC unit is larger than 9, the ionic conductivity then decreases. It is suggested that with the increase in the CC/ED2003 ratios from CEG(5) to CEG(9), i.e., with increasing the chain lengths, the ionic conductivity increases due to both the polymer diffusion and polymer segmental motion/site percolation [20,21]. When the CC unit is larger than 9, however, the chain entanglement occurs which forms dynamic crosslinks between the salt and the polymer and thus reduces the ionic conductivity for the CEG(11) sample [20,21]. Therefore, CC unit of 9 is used for further characterizations of CEG(9)–*X* hybrid electrolytes system.

3.1. Thermal behaviors of the hybrid electrolytes

Crystallinity and flexibility of the polymer matrix are two important factors that affect the behavior of the hybrid electrolytes. Both can be determined by DSC. Fig. 1 shows the DSC thermograms of CEG(9)–*X* hybrid electrolytes with various [O]/[Li] ratios. As seen in Fig. 1, the pure ED2003 exhibits a crystalline melting transition at 35.4 °C. After formation of the hybrid structure, the melting peak slightly shifted to 35 °C. The melting peak shifted to a lower temperature after the addition of salt, and it was continuously decreased with the increase in salt concentration. The CEG(9)–16 sample exhibited the lowest melting temperature of 21 °C. It suggested that the increased interaction of $LiClO_4$ salt with the PEG/PPG unit of polymer gradually shifted the melting peak towards lower temperatures. As the area under the melting endotherm curve is associated with the crystallinity of the materials, the percentage of crystallinity of the hybrid electrolytes is estimated using the equation,

$$\chi_c = \frac{\Delta H}{\Delta H_f} \times 100\% \quad (1)$$

where ΔH_f is the enthalpy of fusion of pure ED2003 (107.4 J g^{-1}) and ΔH is the enthalpy of fusion of the hybrid electrolyte. Table 1 summaries the melting temperature (T_m), ΔH and crystallinity (χ_c) of the hybrid electrolytes with various [O]/[Li] ratios. As seen in Table 1, the endothermic heat decreases with the decrease in the [O]/[Li] ratios, and so as the crystallinity. The decrease in the endothermic heat as well as crystallinity with the decrease in the [O]/[Li] ratios suggest the increased interactions between the ether "O" atoms of PEG/PPG and the Li^+ ions, which inhibit the effective reorganization of the polymer chains for crystallization to occur [22]. An exothermic peak at −15.9 °C, corresponding to the recrystallization of ED2003 was observed for the CEG(9)–24 sample, but it significantly decreased for CEG(9)–16 with a high salt concentration. This observation implied that the recrystallization process was suppressed by the amounts of salt presented in the hybrid materials [23].

Another important property, glass transition temperature (T_g) was also tried to measure from DSC. However, only two T_g values were possible to be obtained for the [O]/[Li] ratios of 24 and 16 due to the instrument's limitation with cooling only down to −60 °C. The values are presented in Table 1. As seen in Table 1, the T_g of the electrolytes increased with the increase in lithium salt concentration. The oxygen atoms of the polyether units interact with lithium cations and enhance the T_g of the electrolytes as the extent of intermolecular interaction increases with the increase in salt concentrations [24].

Table 1
Glass transition temperature (T_g), melting temperature (T_m), enthalpy of fusion (ΔH) and percentage of crystallinity (χ_c) of CEG(9)–*X* solid hybrid electrolytes.

Sample	T_g (°C)	T_m (°C)	ΔH (J g^{-1})	χ_c (%)
Pure ED2003	–	35.4	107.4	100
CEG(9)–∞	–	35.0	86.2	80.2
CEG(9)–48	–	32.6	68.9	64.2
CEG(9)–40	–	31.1	69.2	64.4
CEG(9)–32	–	29.9	59.9	55.8
CEG(9)–24	−47.6	27.4	47.4	44.1
CEG(9)–16	−38.9	21.0	6.6	6.1

3.2. FTIR spectroscopic investigation of the hybrid electrolytes

Infrared spectroscopy is a suitable method to obtain the structural information of the organic–inorganic hybrids as well as the interactions of polyether with the lithium salt. The FTIR spectra of the CEG(9)–*X* solid hybrid electrolytes with various [O]/[Li] ratios are shown in Fig. 2. The broad band observed in the region 3600–3300 cm^{-1} was due to overlapping of the N–H and O–H stretching vibrations [25]. The peak observed around 2875 cm^{-1} was due to the symmetric CH_2 stretching vibration of the polymer [26]. The band at 1648 cm^{-1} was considered to be the C=N

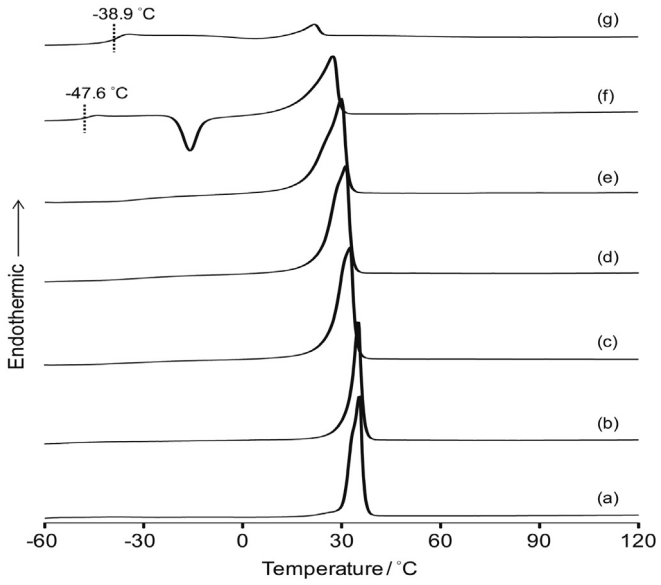

Fig. 1. DSC thermograms of (a) pure ED2003, (b) CEG(9)–∞ membrane, and CEG(9)–*X* solid hybrid electrolytes with *X* = (c) 48, (d) 40, (e) 32, (f) 24, and (g) 16.

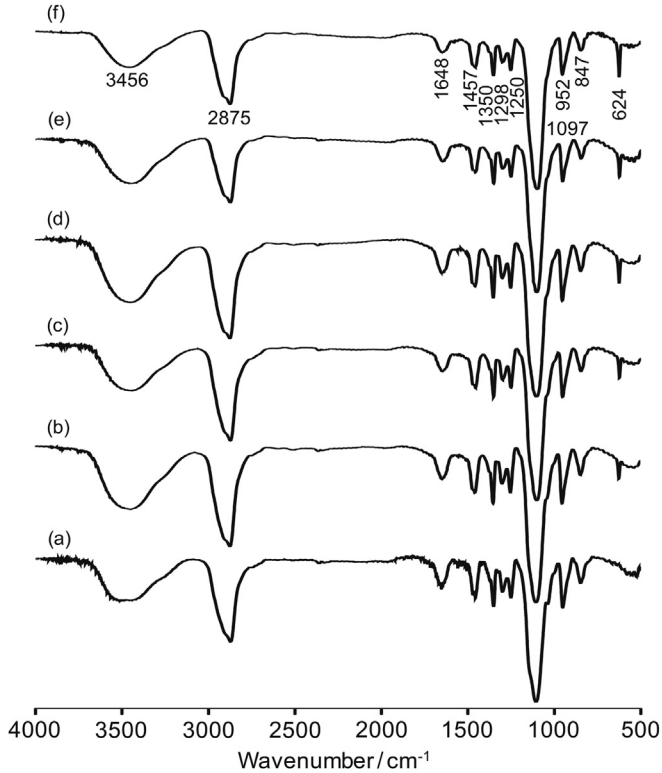

Fig. 2. FTIR spectra of (a) CEG(9)–∞ membrane, and CEG(9)–*X* solid hybrid electrolytes with *X* = (b) 48, (c) 40, (d) 32, (e) 24, and (f) 16.

stretching vibration of the CN groups from the cyanuric chloride unit. The peaks at 1457, 1350, 1298, 1250 and 847 cm^{-1} were assigned to CH_2 bending, wagging, twisting and rocking vibrations of the polymer, respectively [27,28]. A major peak associated with C–O–C stretching vibrations was observed at 1097 cm^{-1} for all the electrolyte samples [16]. In general, the characteristic absorption bands due to Si–O–C and Si–O–Si asymmetric stretching vibrations related to GLYMO were expected to appear in the range of 1110–1030 cm^{-1} [27,29]. As the C–O–C interaction is more dominant than Si–O–C and Si–O–Si and all are closer in absorption frequencies, therefore all of the three vibrations overlapped to give a peak at 1097 cm^{-1}. The absorption peak for $LiClO_4$ can be found at 624–635 cm^{-1}.

The dissociation of salt is an important parameter that affects the ionic movements of the electrolyte. In particular, the characteristic $\nu(ClO_4^-)$ mode of the $LiClO_4$ salt is sensitive to the changes of the ion–ion interactions in the electrolyte system. Two bands centered at 624 and 634 cm^{-1} can be obtained by deconvoluting the broad peak around 600–650 cm^{-1}. The band centered at 624 cm^{-1} can be attributed to the vibration of the "free" ClO_4^- anion, which does not interact directly with the lithium cations, while the band centered at 634 cm^{-1} is due to the vibration of the $Li^+ClO_4^-$ contact-ion pairs [30,31]. To investigate the behavior of ion association in the present hybrid systems, the spectral features of the $\nu(ClO_4^-)$ mode are fitted with Gaussian–Lorentzian functions, and the results are displayed in Fig. S2 (SI). About 96–90% of ClO_4^- existed as spectroscopically "free" species for the CEG(9)–*X* ($X = 48$–24) samples, while about 87% of free ClO_4^- was observed for CEG(9)–16. It suggests that the addition of more salt binds the free ions with the opposite ions to form contact ion pairs, which result in fewer free lithium ions at higher salt concentrations for the cationic transport.

3.3. Polymer and silicate structure analyzed by solid-state NMR

Solid-state ^{13}C and ^{29}Si CPMAS NMR measurements were performed in order to gain more insights into the backbone structure as well as the inorganic part of the CEG(9)–*X* hybrid electrolytes. As shown in Fig. 3A, the most predominant peak at 70.5 ppm is assigned to the methylene carbons adjacent to the ether oxygen of the polymer chain. The methyl carbon from the PPG units appears at 17 ppm, while the peak at 50 ppm can be assigned to the nitrogen substituted carbons at the terminal of the diamines in ED2003. Two peaks at 22 and 9 ppm are assigned to the methylene carbons in the α and β positions to the silicon atom of GLYMO. The ^{13}C signal at 160 ppm due to the central core CC is too weak to be observed, since the CC amount is much less as compared to the other components in the materials. There is a smaller peak at 75 ppm due to the ether carbons in the PPG segments. The ^{13}C CPMAS NMR observations are consistent with the hybrid structure as shown in Scheme 1.

^{29}Si CPMAS NMR measurements were carried out to investigate the silicate framework inside the organic–inorganic hybrid electrolytes. As shown in Fig. 3B, two signals at −68.1 and −58.1 ppm, corresponding to T^3 ($RSi(OSi)_3$, R = alkyl group) and T^2 ($RSi(OSi)_2(OH)$) sites, are observed for the CEG(9)–32 hybrid electrolyte. The observation of *T* groups confirms the presence of organosilane groups in the hybrid electrolyte samples. As the percentage of T^3 (80%) is higher than T^2 (20%), it indicates that a high degree of silica condensation is formed by the inorganic hybrid in the hybrid electrolytes.

3.4. Ionic conductivity of solid hybrid electrolytes

Fig. 4 shows the temperature dependence of the ionic conductivity of the CEG(9)–*X* solid hybrid electrolytes with various [O]/[Li] ratios. The solid CEG(9)–*X* system exhibited a non-linear variation of conductivity with the temperature. Generally, the ionic conductivity (σ) of a polymer electrolyte depends on the actual concentration of the conducting species and their mobility as

$$\sigma(T) = \sum_i n_i q_i \mu_i \quad (2)$$

where n_i is the number of charge carriers, q_i is the charge on each charge carrier, and μ_i is the mobility of charge carriers. As seen in Fig. 4, the ionic conductivity increases with the increase in salt concentration up to CEG(9)–32 and then it decreases with higher salt concentrations. Although the total number of charge carriers increase with increasing salt concentrations, the associated ionic species, such as, contact ion pairs and ion aggregates also increase with the increase in salt concentration, which reduces the overall mobility and the number of effective charge carriers. Consequently, a decrease in ionic conductivity is often observed at high salt concentrations [32]. Moreover, as seen in Fig. 4, the ionic conductivity increases with the increase in temperature. The behavior of enhancement in ionic conductivity can be explained with the free volume theory proposed by Cohen and Turnbull [33]. When the temperature is increased, the polymer chains become more flexible and expand easily to create free volumes. Therefore, the ions, solvated molecules, or the polymer segments can move into the free volume and travel freely and faster which helps in the enhancement of ionic conductivity. The CEG(9)–32 sample exhibits the maximum ionic conductivity value of 1.6×10^{-4} S cm^{-1} at 30 °C, which is the highest ever ionic conductivity value reported on this kind of hybrid electrolytes to the best of our knowledge [17,19,34–37]. When the temperature is over 55 °C, however, the ionic conductivity values of CEG(9)–32 are lower than the CEG(9)–24 and CEG(9)–16 samples with higher salt contents. The ionic conductivity values for CEG(9)–32, CEG(9)–24, CEG(9)–16 are 7.7×10^{-4}, 9.4×10^{-4}, and 9.1×10^{-4} S cm^{-1}, respectively, at 80 °C. Since the charge carrier concentration is higher for CEG(9)–24 and CEG(9)–16, these charge carriers can have enough free space to move freely with the increase in the free volume, and thereby possess higher ionic conductivity values than that of CEG(9)–32 at higher temperatures. In addition, the plots of ionic conductivity vs. temperature are curve like, indicating the VTF (Vogel–Tamman–Fulcher) type behavior. Although the curve profile necessitated to interpret the data with the VTF equation, it was not possible to fit in the VTF equation, as the T_g values of the most of the hybrid electrolytes were not possible to measure due to the limitation of our DSC instrument for measurements below −60 °C. The plots nature of the VTF like behavior suggests that there is a significant amount of segmental chain mobility at higher temperatures for the electrolyte samples to enhance the ionic conductivity to the present level. Therefore, all the factors (i.e., total number of charge carriers, free ions, segmental mobility, free volume) act in a cooperative fashion to make CEG(9)–32 the best ion conductive sample in this organic–inorganic hybrid electrolyte system.

3.5. ^7Li linewidth measurements

The lithium ion mobility can be determined from ^7Li solid-state static NMR as a function of temperature. The static ^7Li linewidths, measured with and without ^1H decoupling, were investigated as a function of temperature from −90 to 90 °C for the CEG(9)–32 and CEG(9)–16 samples. As shown in Fig. 5, the static ^7Li NMR linewidth evolution as a function of temperature for the two selected samples exhibit similar shapes, and can be described by a curve composed of two plateaus separated by a temperature range where a rapid change in line widths occurred. At low temperatures

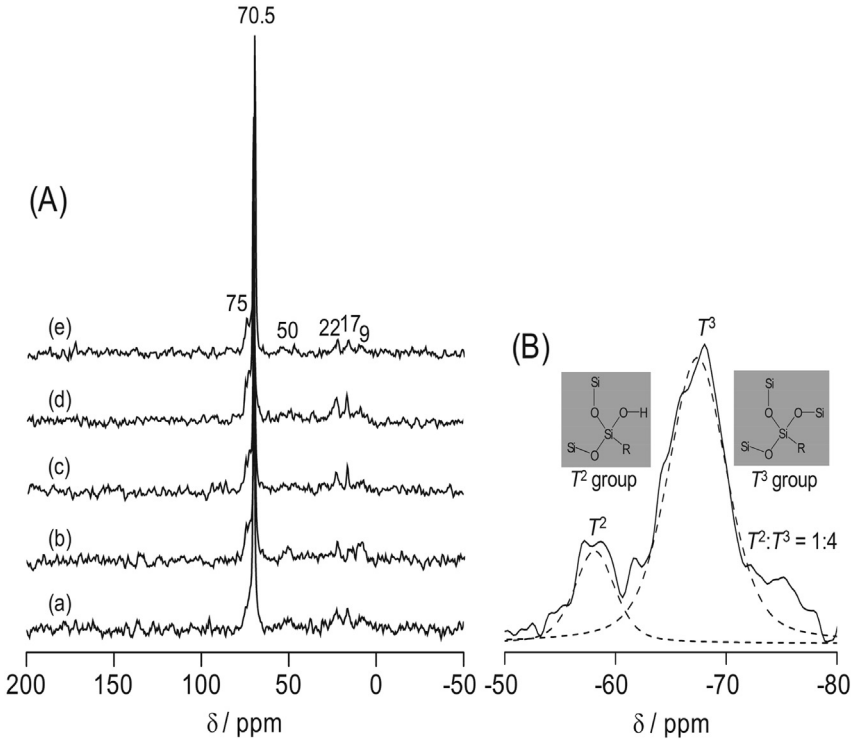

Fig. 3. (A) ^{13}C CPMAS NMR spectra of CEG(9)–*X* solid hybrid electrolytes with *X* = (a) 48, (b) 40, (c) 32, (d) 24, and (e) 16. (B) ^{29}Si CPMAS NMR spectrum of CEG(9)–32 solid hybrid electrolyte.

(<−40 °C), below the T_g of the systems, the linewidths were very broad (FWHH = ~5 kHz) and slightly narrowed upon increasing the temperature, indicating the limited motion of the lithium cation at low temperatures. A significant reduction in the ^{7}Li linewidth (from 5.0 to 1.0 kHz) in the low temperature region (i.e., −90 to −40 °C) was achieved by the use of the proton decoupling techniques. The phenomena demonstrated that the linewidth of ^{7}Li NMR spectra is predominately governed by ^{1}H–^{7}Li dipolar interactions. This is consistent with the fact that for the nuclear spin $I > 1/2$ with a relatively small quadrupolar moment such as the ^{7}Li nucleus, the central transition line width is primarily determined by the dipole–dipole interactions [38]. The residual linewidth of 1.0 kHz in the

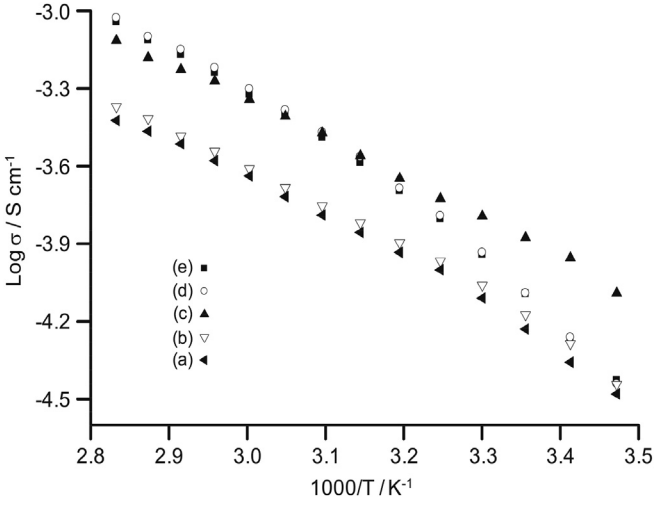

Fig. 4. Temperature dependence of the ionic conductivity of CEG(9)–*X* solid hybrid electrolytes with *X* = (a) 48, (b) 40, (c) 32, (d) 24, and (e) 16.

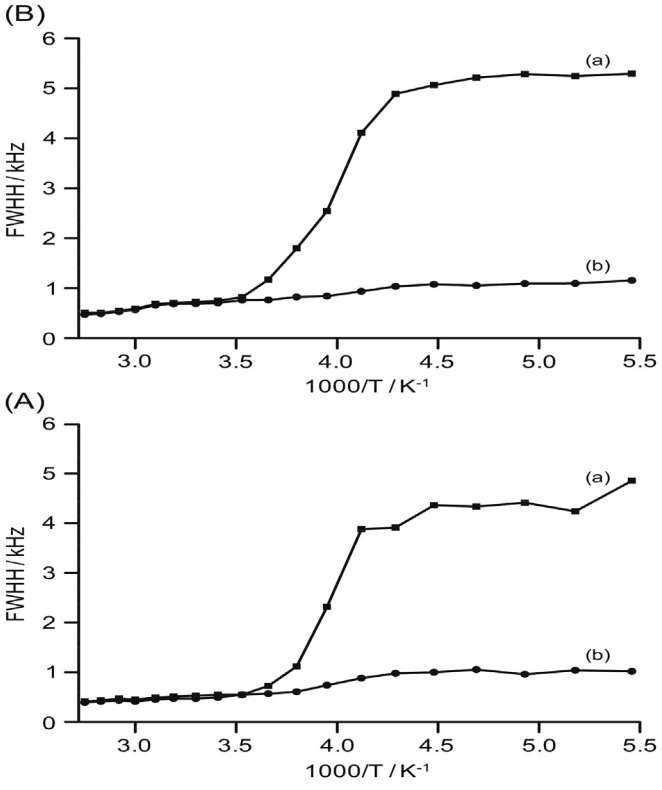

Fig. 5. Temperature dependence of the ^{7}Li static linewidths of CEG(9)–*X* solid hybrid electrolytes with the [O]/[Li] ratio of (A) 32 and (B) 16, measured (a) without and (b) with proton decoupling.

proton decoupled ^{7}Li static NMR spectra is mainly due to the ^{7}Li–^{7}Li homonuclear interactions and/or ^{7}Li quadrupolar interactions. Upon increasing the sample temperature, the linewidths are motionally narrowed. At high temperatures, the linewidth of CEG(9)–32 and CEG(9)–16 is about 0.39 and 0.47 kHz, respectively. Motional narrowing of the ^{7}Li cations begins when the rate of fluctuations of either the local dipolar fields or the electric field gradients is comparable to their respective rigid lattice linewidths [39]. Thus, the Li ions are mobile near the onset temperature of motional narrowing.

3.6. Transformation of solid hybrid electrolytes to plasticized hybrid electrolytes

Although the present solid hybrid electrolytes are suitable for some electrochemical applications, it is not possible to use in lithium ion batteries due to their lower ionic conductivity values. To explore the possibility of the present hybrid electrolyte system to be applied in lithium ion batteries, attempt was therefore made to plasticize the solid salt free hybrid polymer membrane, that is, CEG(9)–∞, with different organic electrolyte solvents to enhance the ionic conductivity. Some necessary characterizations were conducted for both parent solid hybrid electrolyte and the resultant plasticized hybrid electrolyte with the purposes to evaluate their potentials in applications of electrochromic devices and lithium ion batteries, respectively.

3.7. Swelling behavior and ionic conductivity of plasticized hybrid electrolytes

The salt free CEG(9)–∞ hybrid sample was used for the swelling ratio (SR) measurements. The swelling ratio of the CEG(9)–∞ hybrid membrane was measured in different electrolyte solvents using the relation,

$$SR(\%) = \frac{W - W_0}{W_0} \times 100 \quad (3)$$

where W and W_0 are the weights of the wet and dry hybrid polymer membrane, respectively. Fig. 6A depicts the swelling behavior of CEG(9)–∞ in different electrolyte solvents. As seen in Fig. 6A, the maximum swelling ratio of 768% was obtained with the 1 M LiOTf in EC/PC (1:1, v/v) after swelling for 100 min. All the electrolyte solvents showed a swelling ratio of over 730% with CEG(9)–∞ after a swelling time of 100 min. The high values of swelling ratio suggest good porosity of the hybrid membrane. Further dipping the hybrid membrane in electrolyte solvents causes extrusion of electrolytes from the membrane. The prolonged dipping time in electrolyte solvents makes the plasticized electrolyte membrane fragile. Therefore, a dipping time of about 60 min is used to measure the ionic conductivity of the plasticized hybrid electrolyte membranes as the value of swelling ratios are close to their saturation values and the electrolyte membranes are mechanically stable.

The temperature dependence of ionic conductivity of the CEG(9)–∞ hybrid electrolytes swelled in different electrolyte solvents are displayed in Fig. 6B. The plasticized hybrid electrolyte shows an Arrhenius-like enhancement of conductivity when the temperature is increased, indicating that ion transport is decoupled from the polymer segmental motion. The maximum ionic conductivity of 6.5×10^{-3} S cm^{-1} was achieved for the plasticized hybrid electrolyte with 1 M $LiPF_6$ in EC/DEC at 30 °C. The high ionic conductivity for the CEG(9)–∞ sample with 1 M $LiPF_6$ in EC/DEC is mainly attributed to the high electrolyte uptake in comparison to other samples as observed from the values of swelling ratio at 60 min. In addition, the dielectric constants and viscosity of the solvents play a distinctive role in achieving such conductivity values. The liquid electrolyte is believed to be entrapped in the pores of the polymer matrix and then penetrated into the polymer chains for swelling the amorphous domains [40,41]. Therefore, lithium ions can travel faster through the liquid electrolyte entrapped pores and amorphous domains to provide high ionic conductivity for this plasticized hybrid electrolyte system. The CEG(9)–∞ plasticized hybrid electrolyte with 1 M $LiPF_6$ in EC/DEC reached ionic conductivity value as high as 10^{-2} S cm^{-1} at 60 °C, which will be beneficial for applications in high temperature batteries.

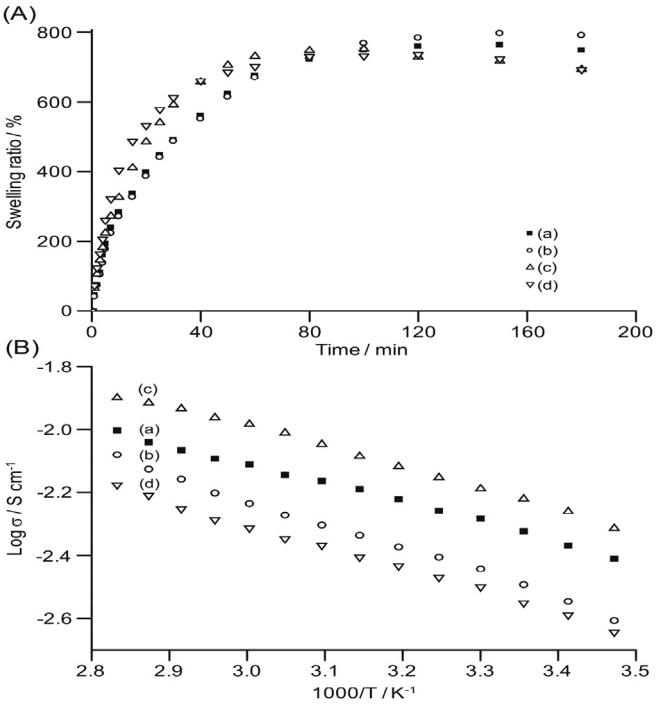

Fig. 6. (A) Swelling ratio and (B) temperature dependence of the ionic conductivity of CEG(9)–∞ plasticized hybrid membrane in different electrolyte solvents: (a) 1 M $LiClO_4$ in EC/PC (1:1 v/v), (b) 1 M LiOTf in EC/PC (1:1 v/v), (c) 1 M $LiPF_6$ in EC/DEC (1:1 v/v) and (d) 1 M LiTFSI in EC/PC (1:1 v/v).

3.8. Electrochemical stability

Electrochemical stability of hybrid electrolytes is a crucial parameter to gauge the electrolytes' performance in electrochemical devices. Electrochemical stability of both solid and plasticized hybrid electrolytes was measured by the linear sweep voltammetry method. The linear sweep voltammograms of Li/hybrid electrolytes/SS cells at a scan rate of 1 mV s^{-1} from 0 to 6 V vs. Li/Li^{+} are shown in Fig. S3 (SI). The electrochemical stability windows were measured for the solid CEG(9)–*X* hybrid electrolytes by varying the [O]/[Li] ratios, and for the plasticized CEG(9)–∞ hybrid electrolytes made by different organic electrolyte solvents. A very low background current was observed in the potential region between 2.0 and 4.2 V for both the hybrid electrolyte systems. A considerable current began to flow when it crossed 4.2 V, indicating the onset of the electrolyte decomposition process. This suggests that both the hybrid electrolytes are electrochemically stable up to 4.2 V, which is sufficient for application in some electrochemical devices.

3.9. Performance of prototype electrochromic device with solid hybrid electrolyte

As the CEG(9)–32 sample provided the maximum ionic conductivity at room temperature, the fabrication and characterization

of the electrochromic device (ECD) was carried out with this hybrid electrolyte.

Light modulation capability of electrochromic devices is expressed by the transmission variation between the colored and bleached states. The active layer of the assembled device changed from almost transparent to a blue color associated with WO_3 reduction and simultaneous Li^+ insertion as a result of the application of a negative voltage. Inversion of the applied voltage resulted in WO_3 oxidation and the device returned to its initial optical state. Fig. 7 illustrates the transmission spectra of as-deposited, bleached and colored states in the range of 300–800 nm for the electrochromic device based on the solid CEG(9)–32 hybrid electrolyte. The spectra were recorded during the 1st coloring/bleaching cycle. As seen in Fig. 7, the electrochromic device provides strong absorption of ultraviolet wavelengths below 320 nm in both colored and bleached states. The average transmittance values in the visible region (400–700 nm) of the as-deposited and bleached states of the ECD are found to be 74% and 67%, respectively. After coloration, the ECD with the solid CEG(9)–32 hybrid electrolyte presents an electrochromic contrast of about 32% and an optical density change [$\Delta(OD) = -\log(T_{colored}/T_{bleached})$] value of 0.28 at the wavelength of 550 nm.

The chronoamperometry data of the ECD fabricated with the CEG(9)–32 hybrid electrolyte up to 4th cycles in the voltage steps between −3 V and +3 V for 50 s is displayed in Fig. S4 (SI). The higher bleaching current arises from the good conductivity of tungsten bronze (H_xWO_3). The 90% full switching time, i.e., the time required for 90% of coloring/bleaching, was measured from the 1st cycle and found to be 17/28 s. Thus, coloring kinetics is faster than bleaching rate.

The coloration efficiency (CE) is the most relevant parameter describing the electrochromic performance of the electrochromic devices and can be defined as the change in optical density per unit of inserted charge, i.e.,

$$CE = \frac{\Delta(OD)}{Q} = \frac{1}{Q} \times \log\left(\frac{T_b}{T_c}\right) = \frac{A_b - A_c}{Q} \quad (4)$$

where Q is the charge density (C cm^{-2}), T_b, T_c and A_b, A_c are the transmittance (T) and absorbance (A) in the bleached and colored states, respectively. The CE value was determined for the ECD with the solid CEG(9)–32 hybrid electrolyte at the 90% of full switch and found to be 183 cm^2 C^{-1} for the 1st cycle. The good value of CE indicates that the ECD exhibits a large optical modulation with a small intercalation charge density, and is a key parameter for practical devices, since the long-term cycling stability is enhanced by using lower charge insertion or extraction. This CE value is comparable to the values reported by other authors on hybrid polymer electrolytes [37,42].

The cycle life is a measure of the number of repetitive color-bleach cycles, which the WO_3 film can sustain without degradation. The cyclic voltammograms of the ECD with the solid CEG(9)–32 hybrid electrolyte were recorded with the linear potential sweep between −3 V and +2.5 V at a scan rate of 30 mV s^{-1} and are shown in Fig. 8 from 10 to 200 cycles. The cathodic coloration peak due to the reduction of WO_3 appears around the extreme value of the applied potential of −3.0 V, while an anodic peak for bleaching is observed around 0.7 V during the oxidation process. Coloration of the device occurs due to insertion of Li^+ ions into the WO_3 layer to form Li_xWO_3. When the voltage polarity is reversed, oxidation occurs with the extraction of lithium ions from Li_xWO_3 and the transparent state of the electrode is restored [19]. As seen in Fig. 8, the cathodic and anodic peak currents of the electrochromic device slowly decrease with the increasing cycles from 10 to 200 cycles. This suggests that the insertion and extraction of lithium that takes place between WO_3 and ITO layers during cycling slowly decreases from 10 to 200 cycles.

3.10. Charge–discharge behavior of plasticized hybrid electrolyte

The plasticized CEG(9)–∞ hybrid electrolyte with 1 M $LiPF_6$ in EC/DEC, which is the most ionic conductive, was used for the charge–discharge testing of the battery cell. The battery was assembled with the lithium metal as the anode and NMC-442 as the cathode. The assembled battery was subjected to the cycle test with an upper voltage limit of 4.0 V and a lower voltage limit of 2.8 V at a current rate of 0.2 C. Fig. 9 shows the discharge behavior and coulombic efficiency of the lithium ion battery up to 30 cycles. The coulombic efficiency of the first cycle was about 95%, which increased to around 96% in-between and finally slightly decreased to 94% at 30 cycles, confirming the almost stable coulombic efficiency values throughout the cycles. The irreversible capacity loss observed in these cycles is caused by the formation of passivation film on the surface of the lithium electrode due to the decomposition of electrolyte. The formation of passivation layer consumes a

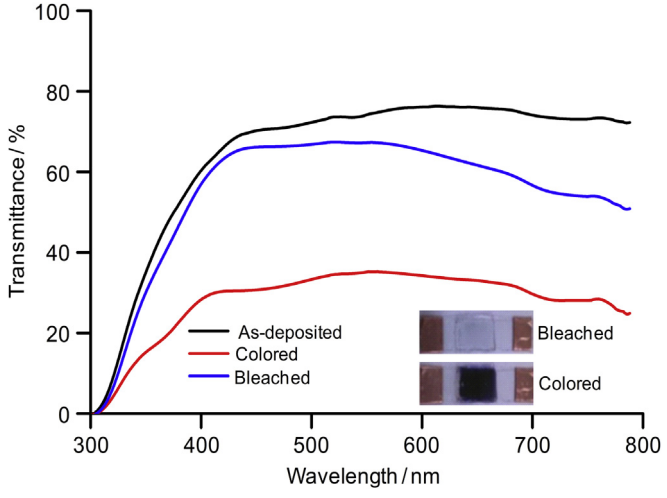

Fig. 7. UV–Vis spectra of the electrochromic device fabricated with CEG(9)–32 solid hybrid electrolyte in the as-deposited (black line), bleached (blue line) and colored (red line) states in the 1st cycle. (For interpretation of the references to color in this figure legend, the reader is referred to the web version of this article.)

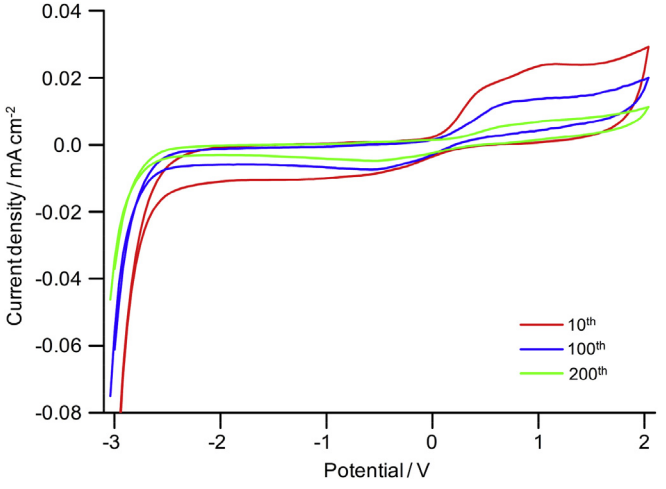

Fig. 8. Cyclic voltammograms of the ECD fabricated with CEG(9)–32 solid hybrid electrolyte at various cycles.

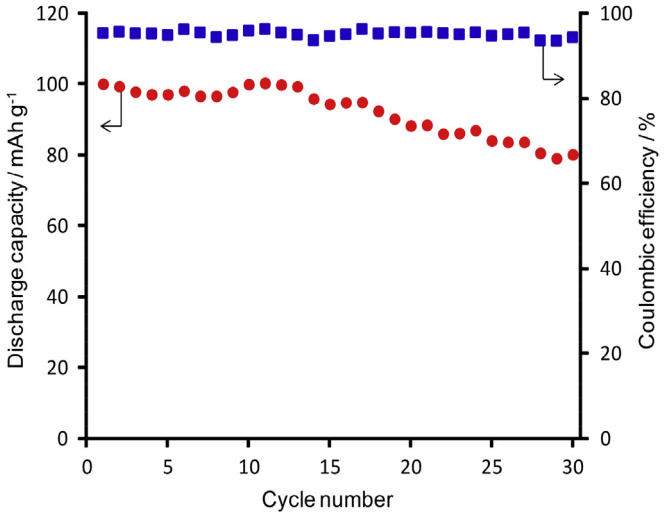

Fig. 9. Discharge capacity and coulombic efficiency of the cell fabricated with CEG(9)–∞ plasticized hybrid electrolyte with 1 M $LiPF_6$ in EC/DEC up to 30 cycles.

part of the anode capacity corresponding to an irreversible capacity loss. The passive layer reduces the charge transfer in the lithium electrode and the diffusion rate of Li^+ ion in the Li/hybrid electrolyte interface becomes very slow.

As observed from the discharge capacity curve in Fig. 9, the initial discharge capacity of the cell is 100 mAh g^{-1} and then slowly decreases to 80 mAh g^{-1} at 30th cycle due to the formation of Li/hybrid electrolyte interface layer [43]. It suggests that the physical changes in the active materials and the passivation film on the surface of the electrode gradually increase the cell internal resistance during the cycling, and block the charge transfer reaction between the Li electrode and the hybrid electrolyte, leading to the discharge capacity loss with cycling. The observed minor fluctuation in discharge capacity values with cycle numbers may be due to the unstable and non-uniform solid electrolyte interphase (SEI) layer.

4. Conclusions

A new type of highly ion conductive organic–inorganic hybrid polymer electrolytes was synthesized by controlling the backbone chain lengths of the polymer matrix. The hybrid electrolytes achieved the maximum ionic conductivity of 1.6×10^{-4} S cm^{-1} in the solid state (i.e., solvent free) and 6.5×10^{-3} S cm^{-1} in the plasticized state (i.e., with organic electrolyte solvents) at 30 °C. The synthesized hybrid can be used as a versatile matrix to prepare both solid and plasticized hybrid electrolytes. Their abilities to be used in electrochromic devices and lithium ion batteries are well demonstrated in this work. The electrochromic device with the solid hybrid electrolyte exhibited a coloration efficiency of 183 cm^2 C^{-1} and a good cycle life. The lithium ion battery with the plasticized hybrid electrolyte carried an initial discharge capacity value of 100 mAh g^{-1} and a coulombic efficiency of about 95% up to 30 cycles. The capabilities and properties exhibited by the present organic–inorganic hybrid polymer electrolytes will be of immense interest to be used in future electrochromic and power storage devices.

Acknowledgments

The authors gratefully acknowledge the financial support from the Ministry of Science and Technology of Taiwan under the grant number NSC 102-2113-M-008-006-MY3.

Appendix A. Supplementary data

Supplementary data related to this article can be found at http://dx.doi.org/10.1016/j.jpowsour.2014.06.159.

References

[1] D.G. Kim, J. Shim, J.H. Lee, S.J. Kwon, J.H. Baik, J.C. Lee, Polymer 54 (2013) 5812–5820.
[2] W. Kwon, Y.J. Chang, Y.C. Park, H.M. Jang, S.W. Rhee, J. Mater. Chem. 22 (2012) 6027–6031.
[3] M.F. Hsueh, C.W. Huang, C.A. Wu, P.L. Kuo, H. Teng, J. Phys. Chem. C 117 (2013) 16751–16758.
[4] C.A. Nguyen, S. Xiong, J. Ma, X. Lu, P.S. Lee, Phys. Chem. Chem. Phys. 13 (2011) 13319–13326.
[5] D.E. Fenton, J.M. Parker, P.V. Wright, Polymer 14 (1973) 589.
[6] M.B. Armand, M.J. Duclot, P. Rigaud, Solid State Ionics 3–4 (1981) 429–430.
[7] A. Balducci, S.S. Jeong, G.T. Kim, S. Passerini, M. Winter, M. Schmuck, G.B. Appetecchi, R. Marcilla, D. Mecerreyes, V. Barsukov, V. Khomenko, I. Cantero, I. De Meatza, M. Holzapfel, N. Tran, J. Power Sources 196 (2011) 9719–9730.
[8] J. Li, I.M. Khan, Macromolecules 26 (1993) 4544–4550.
[9] O.V. Bushkova, V.M. Zhukovsky, B.I. Lirova, A.L. Kruglyashov, Solid State Ionics 119 (1999) 217–222.
[10] A. Asghar, Y.A. Samad, B.S. Lalia, R. Hashaikeh, J. Membr. Sci. 421–422 (2012) 85–90.
[11] A. Nishimoto, M. Watanabe, Y. Ikeda, S. Kohjiya, Electrochim. Acta 43 (1998) 1177–1184.
[12] B.W. Zewde, S. Admassie, J. Zimmermann, C.S. Isfort, B. Scrosati, J. Hassoun, ChemSusChem 6 (2013) 1400–1405.
[13] L.M. Bronstein, R.L. Karlinsey, K. Ritter, C.G. Joo, B. Stein, J.W. Zwanziger, J. Mater. Chem. 14 (2004) 1812–1820.
[14] S.C. Nunes, V. de Zea Bermudez, M.M. Silva, S. Barros, M.J. Smith, E. Morales, L.D. Carlos, J. Rocha, Solid State Ionics 176 (2005) 1591–1599.
[15] D.M. Tigelaar, M.A.B. Meador, J.D. Kinder, W.R. Bennett, Macromolecules 39 (2006) 120–127.
[16] H.-M. Kao, T.-T. Hung, G.T.K. Fey, Macromolecules 40 (2007) 8673–8683.
[17] D. Saikia, Y.-H. Chen, Y.-C. Pan, J. Fang, L.-D. Tsai, G.T.K. Fey, H.-M. Kao, J. Mater. Chem. 21 (2011) 10542–10551.
[18] J.Z. Jan, B.H. Huang, J.-J. Lin, Polymer 44 (2003) 1003–1011.
[19] D. Saikia, Y.-C. Pan, C.-G. Wu, J. Fang, L.-D. Tsai, H.-M. Kao, J. Mater. Chem. C (2014) 331–343.
[20] J. Shi, C.A. Vincent, Solid State Ionics 60 (1993) 11–17.
[21] A.A. Teran, M.H. Tang, S.A. Mullin, N.P. Balsara, Solid State Ionics 203 (2011) 18–21.
[22] J. Xi, X. Qiu, X. Ma, M. Cui, J. Yang, X. Tang, W. Zhu, L. Chen, Solid State Ionics 176 (2005) 1249–1260.
[23] W.A. Henderson, Macromolecules 40 (2007) 4963–4971.
[24] J.F. Le Nest, A. Gandini, C. Schoenenberger, Trends Polym. Sci. 2 (1994) 432–437.
[25] M.M. Coleman, K.H. Lee, D.J. Skrovanek, P.C. Painter, Macromolecules 19 (1986) 2149–2157.
[26] L.S. Teo, C.Y. Chen, J.F. Kuo, Macromolecules 30 (1997) 1793–1799.
[27] P. Patnaik, Dean's Analytical Chemistry Handbook, second ed., McGraw-Hill, New York, 2004, pp. 7.1–7.43.
[28] D.L. Pavia, G.M. Lampman, G.S. Kriz, Introduction to Spectroscopy, Harcourt College Publication, USA, 2001, pp. 15–84.
[29] A. Kioul, L. Mascia, J. Non-Cryst. Solids 175 (1994) 169–186.
[30] M. Salomon, M. Xu, E.M. Eyring, S. Petrucci, J. Phys. Chem. 98 (1994) 8234–8244.
[31] H.-W. Chen, C.-Y. Chiu, H.-D. Wu, I.-W. Shen, F.-C. Chang, Polymer 43 (2002) 5011–5016.
[32] W.A. Henderson, J. Phys. Chem. B 110 (2006) 13177–13183.
[33] M.H. Cohen, D. Turnbull, J. Chem. Phys. 31 (1959) 1164–1169.
[34] P.C. Barbosa, M.M. Silva, M.J. Smith, A. Gonçalves, E. Fortunato, S.C. Nunes, V. de Zea Bermudez, Electrochim. Acta 54 (2009) 1002–1009.
[35] S.C. Nunes, V. de Zea Bermudez, D. Ostrovskii, M.M. Silva, S. Barros, M.J. Smith, L.D. Carlos, J. Rocha, E. Morales, J. Electrochem. Soc. 152 (2005) A429–A438.
[36] D. Saikia, H.-Y. Wu, C.-P. Lin, Y.-C. Pan, J. Fang, L.-D. Tsai, G.T.K. Fey, H.-M. Kao, Polymer 53 (2012) 6008–6020.
[37] P.C. Barbosa, M. Fernandes, S.M.F. Vilela, A. Gonçalves, M.C. Oliveira, E. Fortunato, M.M. Silva, M.J. Smith, R. Rego, V. de Zea Bermudez, Int. J. Electrochem. Sci. 6 (2011) 3355–3374.
[38] N.C. Mello, T.J. Bonagamba, H. Panepucci, K. Dahmouche, P. Judeinstein, M.A. Aegerter, Macromolecules 33 (2000) 1280–1288.
[39] S.H. Chung, K.R. Jeffrey, J.R. Stevens, J. Chem. Phys. 94 (1991) 1803–1811.
[40] Y. Saito, H. Kataoka, E. Quartarone, P. Mustarelli, J. Phys. Chem. B 106 (2002) 7200–7204.
[41] Z. Li, G. Su, X. Wang, D. Gao, Solid State Ionics 176 (2005) 1903–1908.
[42] P.C. Barbosa, L.C. Rodrigues, M.M. Silva, M.J. Smith, A.J. Parola, F. Pina, C. Pinheiro, Electrochim. Acta 55 (2010) 1495–1502.
[43] H.-H. Kuo, W.-C. Chen, T.-C. Wen, A. Gopalan, J. Power Sources 110 (2002) 27–33.